Impact of Ca substitution on competing orders in superconducting $BaNi_2As_2$

F. Henssler,[1] K. Willa,[1] M. Frachet,[1,2] T. Lacmann,[1] D. A. Chaney,[3] R. Heid,[1] M. Merz,[1,4] A.-A. Haghighirad,[1,*] and M. Le Tacon[1,†]

[1]*Institute for Quantum Materials and Technologies, Karlsruhe Institute of Technology, Kaiserstr. 12, D-76131 Karlsruhe, Germany*
[2]*CEA-Leti, Université Grenoble Alpes, 17 avenue de Martyrs, F-38054 Grenoble, France*
[3]*ESRF, The European Synchrotron, 71 avenue des Martyrs, CS 40220 F-38043 Grenoble Cedex 9, France*
[4]*Karlsruhe Nano Micro Facility (KNMFi), Karlsruhe Institute of Technology, Kaiserstr. 12, D-76131 Karlsruhe, Germany*

(Received 28 November 2024; revised 26 February 2025; accepted 25 March 2025; published 2 April 2025)

$BaNi_2As_2$, a structural analog to the iron-based parent compound $BaFe_2As_2$, offers a unique platform to study the interplay between superconductivity, charge density waves, and, possibly, electronic nematicity. Here, we report on the growth and characterization of $Ba_{1-x}Ca_xNi_2As_2$ single crystals with $0 \leqslant x \leqslant 0.1$, using a combination of x-ray diffraction, diffuse x-ray scattering, heat capacity, and electronic transport measurements. Our results demonstrate that calcium substitution affects the structural, electronic, and thermodynamic properties of $BaNi_2As_2$ in a way that is strongly reminiscent of moderate hydrostatic pressures albeit with marked differences. In particular, Ca substitution efficiently suppresses both the triclinic structural transition and the associated commensurate charge density wave formation, while increasing the superconducting transition temperature. We found that the substitution range in which the crystals remain homogeneous is limited with concentrations $x \geqslant 0.04$ exhibiting intense diffuse x-ray scattering indicative of stacking fault formation, which, despite the preserved integrity of the NiAs layers, prevents investigation up to concentrations where chemical pressure is expected to completely suppress the structural instability.

DOI: 10.1103/PhysRevMaterials.9.044801

I. INTRODUCTION

The coexistence of magnetically or charge-ordered phases with superconductivity is a common feature in the complex phase diagrams of quantum materials. A major challenge in this field is to unravel the nature of the interplay between these electronic phases [1]. This is crucial for understanding unconventional superconductivity, where the emergent properties of quantum materials often depend on a delicate balance and interplay of different electronic orders. This balance can be experimentally tuned using controllable parameters such as pressure, strain, magnetic field, or charge carrier concentration [2]. Chemical substitution is one of the most widely used and effective methods for exploring the electronic landscape of unconventional superconducting materials, including high-temperature superconducting cuprates [3] and iron-based superconductors [4]. The present work focuses on the superconducting compound $BaNi_2As_2$ [5], which at room temperature shares the $ThCr_2Si_2$ tetragonal *I4/mmm* crystal structure with $BaFe_2As_2$, the parent compound of iron-based superconductors. However, $BaNi_2As_2$ exhibits a very different electronic phase diagram. Recently, it has attracted significant attention for hosting multiple charge density waves (as opposed to magnetic phases, which have not been detected so far) combined with structural distortions [6–13]. The interplay between these features and the superconducting phase remains elusive. Earlier studies of $BaNi_2As_2$ revealed a strong first-order structural transition to a triclinic ($P\bar{1}$) phase below $T_S = 135\,\mathrm{K}$ (upon cooling), followed by a low-temperature superconducting instability at $T_c = 0.6\,\mathrm{K}$, presumably of conventional BCS type [14]. More recently, it was discovered that a long-range commensurate charge density wave (C-CDW) with a characteristic wave vector of $q = (1/3\,0\,-1/3)_{\mathrm{tet}}$ (for simplicity, all reciprocal space wave vector are given in the tetragonal notation $(H\,K\,L)_{\mathrm{tet}}$, but the subscript "tet" will be omitted) forms in the triclinic phase [6]. Additionally, the existence of an incommensurate and uniaxial charge density wave (I-CDW) at $q = (0.28\,0\,0)$ above the triclinic transition was reported and investigated in detail [6,8]. Precursor diffuse x-ray scattering linked to this I-CDW has been observed even at room temperature and is associated with soft-phonon modes that condense upon cooling [12,13] and yield a long-range I-CDW order and a small B_{1g}-symmetric orthorhombic (*Immm*) distortion below $\sim$142 K [8,9]. The electronic phase diagram of $BaNi_2As_2$ has been explored using hydrostatic pressure [11,15] and various isoelectronic chemical substitutions [7–9,16–18]. Interestingly, irrespective of the crystallographic site on which these substitutions occur, T_S decreases and, as the C-CDW gets eventually completely suppressed, a sudden increase of the superconducting transition temperature T_c to $\sim$ 3.5 K [9,16,17] occurs. The origin of

*Contact author: amir-abbas.haghighirad@kit.edu
†Contact author: matthieu.letacon@kit.edu

this behavior is still debated. On the one hand, a recent study on the Sr-substituted compound $Ba_{1-x}Sr_xNi_2As_2$ revealed the presence of a novel C-CDW with $q = (0\,1/2\,1/2)$ [7], while electrical resistivity measurements under strain were interpreted as evidence of electronic nematicity in the normal state of this compound and suggested that the enhancement of T_c could occur through nematic fluctuations [7,17]. On the other hand, elastoresistivity and thermodynamic investigations in phosphorus-substituted samples revealed an overall different (but equally rich) phase diagram [9,10,18], in which unusual nematic fluctuations are reported but also point to an absence of nematic criticality. Instead, these studies associate the increase of T_c to an enhancement of the electron-phonon coupling in a more conventional electron-phonon pairing mechanism [5,16,19,20].

The available data indicate that the electronic phase of $BaNi_2As_2$ is particularly sensitive to the lattice parameter ratio c/a [9], and the different behavior may be related to the fact that this ratio is affected very differently by the different types of substitutions. Indeed, crystallographic data show that substituting Ba with Sr in $Ba_{1-x}Sr_xNi_2As_2$ yields a monotonic decrease of the c/a ratio from 2.81 in pristine $BaNi_2As_2$ (at room temperature) to 2.45 in $SrNi_2As_2$, effectively resulting in a strong uniaxial c-axis chemical pressure. On the contrary, c/a remains essentially constant in the case of substitution of As with P [9]. Furthermore, it is worth noting that whereas only ∼0.07 of P substitution for As is needed to completely suppress the triclinic phase [9,16,17,21], no less than ∼0.7 of Sr on the Ba site is required to obtain the same effect. These disparities highlight that beyond chemical pressure, substitution could also significantly impact the electronic properties of $BaNi_2As_2$ through, e.g., the introduction of disorder, calling in turn for careful studies of the evolution of lattice and electronic degrees of freedom of $BaNi_2As_2$ under chemical substitution.

In this work, we explore the alternative isovalent substitution of Ba with Ca rather than with Sr. In the 122 Fe-based family, the electronic properties of $CaFe_2As_2$ exhibit an unusually strong pressure dependence. A moderate hydrostatic pressure of ∼0.35 GPa can turn the low-temperature antiferromagnetic orthorhombic phase into a nonmagnetically ordered collapsed tetragonal structure with a dramatic decrease of the unit cell volume by 0.05 and of the c/a ratio by 0.11 [22]. In the $CaNi_2As_2$ end member of the nickel series, the c/a ratio of the tetragonal unit cell is similar to that of $SrNi_2As_2$, albeit with a significant reduction of the total unit cell volume (from 177.6 $Å^3$ in $SrNi_2As_2$ to 164 $Å^3$ in $CaNi_2As_2$ [23]). This also suggests that a complete suppression of the triclinic/C-CDW phases could be achieved with lower substitution levels using Ca instead of Sr.

We report on the crystal structure and characterization of the basic electronic properties of $Ba_{1-x}Ca_xNi_2As_2$ single crystals up to $x \sim 0.1$. High-quality homogeneous single crystals were successfully synthesized for Ca concentrations up to $x \sim 0.04$, with concentrations determined using energy-dispersive x-ray spectroscopy (EDX) or x-ray diffraction (XRD), depending on the measurement method. The structural and electronic properties of the crystals were characterized using XRD, diffuse x-ray scattering (DS), EDX, electrical transport, and heat capacity measurements. At higher Ca concentrations, we find a strong compression of the a-axis parameter, however, the crystals tend to be less homogeneous, and reciprocal space reconstructions reveal long streaks along the reciprocal L directions, a characteristic signature of stacking faults. We find that 0.09 of Ca substitution suppresses the triclinic phase transition temperature down to approximately 100 K (which would require ∼0.5 of Sr) and increases the superconducting transition temperature by ∼0.5. In the investigated Ca-concentration range, the substitution yields a compression of lattice parameters similar to those obtained under hydrostatic pressure up to ∼1.5 GPa [11]. It also has a similar impact on the incommensurability of the I-CDW ($q_{\text{I-CDW}}$ slightly increases). First-principle calculations of the electronic structure confirm that hydrostatic pressure and Ca substitution have similar effects on several Fermi surface sheets, including a Fermi surface pocket whose suppression upon Sr substitution has recently been associated with the enhancement of nematic fluctuations and optimal superconducting T_c in these materials [24]. In contrast with hydrostatic pressure, no additional CDW phase nor structural distortion were observed in the investigated substitution range, as summarized in a first phase diagram of $Ba_{1-x}Ca_xNi_2As_2$.

TABLE I. Growth parameters varied between the different batches.

$x_{\text{Ca,nom}}$	T_{max}(°C)	t_{dwell}(h)	r_{cool}(°C/h)
0.05	1150	8	0.80
0.1	1180	8	0.77
0.2	1235	6	0.83
0.3	1235	6	0.80
0.4	1225	6	0.65

II. EXPERIMENTAL METHODS

The $Ba_{1-x}Ca_xNi_2As_2$ single crystals were grown using a self-flux (NiAs) method. All the handling operations were carried out in a glove box under an inert Ar atmosphere ($O_2 < 0.5$ ppm). The precursor NiAs was synthesized by mixing and grinding elemental Ni powder (Alfa Aesar 99.9 %) and As powder (chemPUR 99.9999 %). The mixture was then sealed in an evacuated quartz tube, which was subsequently heated to 730 °C with 50 °C/h. After a dwell time of 20 h it was cooled down to 75 °C with 200 °C/h. The resulting NiAs was then ground to powder and mixed with Ba (lump, Alfa Aesar 99.99 %) and Ca (lump, Alfa Aesar 99.98 %) in the ratio (Ba, Ca):NiAs=1:4. Then, the powder was heated in a glassy carbon or alumina crucible and placed in a sealed fused silica ampule (in a vacuum) with 100 °C/h to 500 °C (dwell time 10 h). The temperature was then increased with 100 °C/h to $T_{\text{max}} = 1150$ to 1235 °C for a dwell time of 6 to 8 h before it was slowly cooled (cooling rate 0.65 to 0.83 °C/h), followed by a decanting of the furnace at 980 °C (see Table I, in which the growth parameters that were varied between the different batches are listed). A picture of a representative sample ($x \sim 0.02$) is shown in Fig. 1(a).

The chemical compositions of the obtained mm-sized single crystals [see Fig. 1(a)] were examined with a COXEM EM-30AXN benchtop device for scanning electron microscopy (SEM) and EDX [Figs. 1(b) and 1(c)], which allows

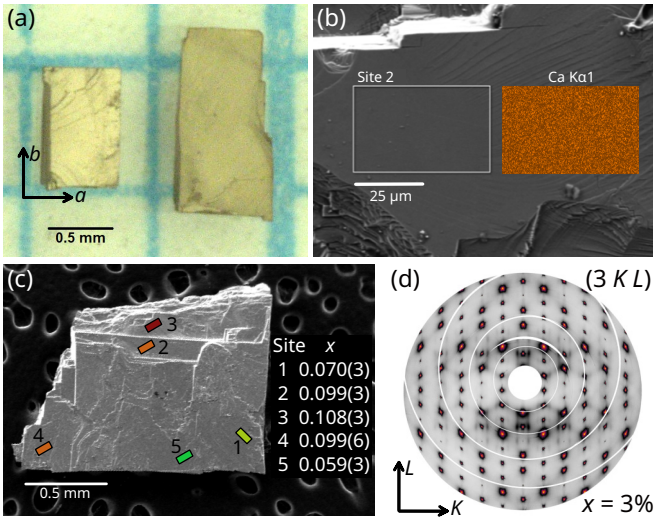

FIG. 1. (a) Typical $Ba_{1-x}Ca_xNi_2As_2$ samples (here, $x \sim 0.02$). The sample sizes range up to $2 \times 2 \times 0.3\,mm^3$. They are well formed in a platelet shape, ideally with rectangular edges and dark surfaces shining with a gold luster. (b) SEM image of a $Ba_{1-x}Ca_xNi_2As_2$ sample, measured at a voltage of 15 kV and a current of 20 nA. On the right side, the intensity distribution of the Ca Kα1 line is depicted. (c) SEM image of a highly substituted $Ba_{1-x}Ca_xNi_2As_2$ sample. Each area is between $50 \times 25\,\mu m^2$ to $100 \times 50\,\mu m^2$ large [see Site 2 in (b)]. The color indicates a substitution level from green ($x \sim 0.06$) to red ($x \sim 0.11$). (d) Reconstruction of the reciprocal space plane ($3\,K\,L$) of an $x = 0.03$ $Ba_{1-x}Ca_xNi_2As_2$ sample, measured at 300 K with diffuse x-ray scattering at the ID28 beamline (ESRF).

the determination of chemical composition with an instrumental accuracy of $\Delta x \gtrsim 1\,\%$, especially for light elements. XRD experiments were conducted using an STOE imaging plate diffraction system (IPDS-2T) utilizing Mo K_α radiation. For the investigated specimens all accessible reflections (≈4600) were measured up to a maximum angle $2\theta = 65^\circ$ at a detector distance of 80 mm. The data were corrected for Lorentz, polarization, extinction, and absorption effects by employing the STOE X-AREA software package. Complementing data sets were collected on our in-house high-flux, high-resolution, rotating anode RIGAKU Synergy-DW (Mo/Ag) diffractometer with Mo K_α radiation. The system is equipped with a background-less Hypix-Arc150° detector, which guarantees minimal reflection profile distortion and ensures uniform detection conditions for all reflections. For these measurements around 8400 reflections were collected in a detector distance of 47 mm and with a resolution up to 0.37 Å, data reduction was performed employing the CrysAlisPro software package [25]. Using SHELXL [26] and JANA2006 [27] all available averaged symmetry-independent reflections ($I > 2\sigma$) have been included for the respective RT refinements in space group $I4/mmm$. The refinements converged well and showed very good weighted reliability factors (wR_2) typically between 4 and 8 %, depending on the mosaic spread and the stacking faults present in the individual samples. Additionally, DS measurements were performed at the ID28 beamline of the European Synchrotron Radiation Facility (ESRF) [28]. The incident photon energy was 17.794 keV, beam size was 40 $\times 40\,\mu m^2$ and the data was recorded using a Pilatus3 X 1M detector in shutterless mode with an angular step of 0.25°. The sample detector distance was 244 mm and data was collected at two detector positions 19 ° and 48 °. Initial analysis was performed using the CrysAlis software package [25] and in-house software developed at the ID28 beamline was employed for high-quality reconstructions of selected reciprocal space layers.

Electrical transport measurements were performed on a Quantum Design Physical Property Measurement System (PPMS) or with a custom setup in an Oxford He-flow cryostat using a Keithley 6221 current source and a Keithley 2182A nanovoltmeter in delta mode. All investigated samples were electrically contacted in a standard four-probe geometry using Pt wires and silver paint (either DuPont 4929N or Hans Wolbring Leitsilber) or silver epoxy (EPO-TEK H20E). Resistance was measured in the *ab* plane with a fixed current of 1 mA and a typical cooling rate of 1 K/min. At low temperature, the applied current was reduced to 0.2 mA.

Specific heat C_p measurements were performed using a PPMS with an He-3 insert. Generally, large heat pulses (temperature rise ∼30 % of the absolute temperature) were evaluated with the dual-slope method except for the region around first-order transitions, where the single-slope method was used. In order to achieve good thermal coupling, the samples were mounted on their edge with a small amount of Apiezon N grease.

III. ELECTRONIC STRUCTURE CALCULATIONS

Density-functional theory calculations of the electronic band structure of $BaNi_2As_2$ and $CaNi_2As_2$ were carried out in the framework of the mixed-basis pseudopotential method [29,30]. As in previous works on $BaNi_2As_2$ (see, e.g., [12]), norm-conserving pseudopotentials of Hamann, Schlüter, Chiang type [31,32] for Ba and of Vanderbilt type [33] for Ca, Ni, and As were used to represent the electron-ion interaction. Semicore states Ba-5p, Ni-3s, Ni-3p, and Ca-3p were included in the valence space. In the mixed-basis approach, valence states are expanded in a combination of plane waves and local functions at atomic sites, which allows an efficient description of more localized components of the valence states. Here, plane waves with a cutoff for the kinetic energy of 22 Ry and local functions of p, d type for Ba and s, p, d type for Ni and Ca, respectively, were employed. The exchange-correlation functional was represented by the general-gradient approximation [34]. Brillouin zone integration was performed by sampling a tetragonal $32 \times 32 \times 16$ k-point mesh in conjunction with a Gaussian broadening of 50 meV. Presented band structures were obtained using experimental structural data taken from [8] for $BaNi_2As_2$ at ambient pressure, from [11] for $BaNi_2As_2$ under pressure ($p = 10.14$ GPa), including a very small monoclinic distortion, and for $CaNi_2As_2$ from [23].

IV. RESULTS

A. Crystal structure and composition

The Ca concentration of the $Ba_{1-x}Ca_xNi_2As_2$ single crystals was determined from EDX measurements and from refinement of the XRD data. We observed that samples

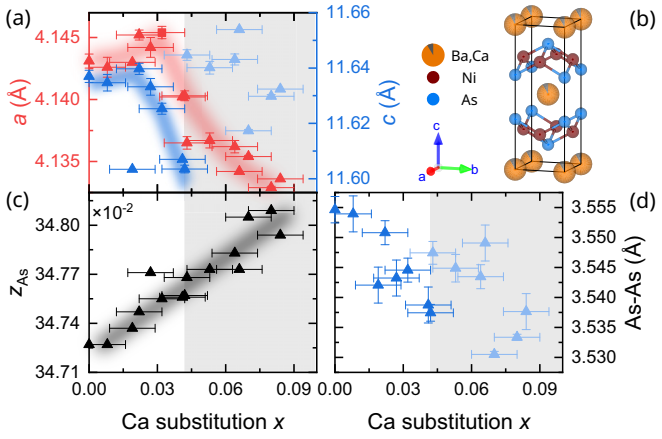

FIG. 2. (a) Substitution dependence of the lattice parameters a and c at room temperature. Samples with Ca concentration $x > 0.04$ (shaded area) were found to have stacking faults that prevented accurate determination of the c-axis lattice parameter (see light blue points). (b) The tetragonal $Ba_{1-x}Ca_xNi_2As_2$ unit cell. (c) The dimensionless z parameter of the Wyckoff position 4e, occupied by As, as a function of the Ca concentration. (d) Substitution dependence of the out-of-plane As-As distance at room temperature. Error bars shown in the plots are statistical errors from the refinements.

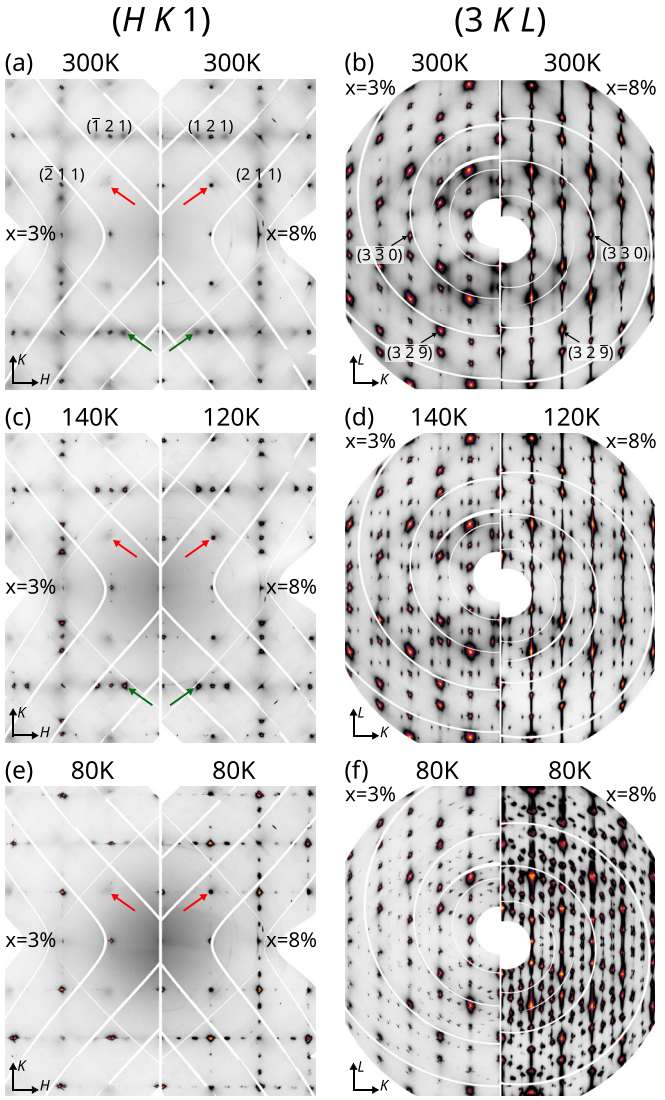

FIG. 3. Reciprocal space planes measured with diffuse x-ray scattering at the ID28 beamline (ESRF). The (H K 1) (a), (c), (e) and ($3\,K\,L$) (b), (d), (f) maps are shown for $x = 0.03$ and $x = 0.08$ for three characteristic temperatures. At room temperature $Ba_{1-x}Ca_xNi_2As_2$ shows weak diffuse scattering at $q = (0.28\,0\,0)$. On cooling, these I-CDW satellite reflections increase dramatically in intensity at about 140 K and 120 K for $x = 0.03, 0.08$, respectively [see green arrows in (a), (c)]. At the base temperature, 80 K, both samples are triclinic (reciprocal maps are shown in the tetragonal unit cell for comparison) and exhibit the C-CDW. In contrast to the lower doped sample, the 0.08 sample shows clear streaks in the ($3\,K\,L$) maps, indicating stacking faults/disorder along the crystallographic c-direction. The (H K 1) maps, which are perpendicular to the (3 K L), naturally show these streaks as a weaker additional peak at a symmetry-forbidden position [see red arrows in (a), (c), (e)].

containing less than 4 % of Ca ($x \leqslant 0.04$) were typically homogeneous and that the Ca concentration from sample to sample was found to be largely constant within the batch. The Ca determination was accurate with EDX and XRD values in close agreement. Room temperature in-house XRD and synchrotron DS measurements confirmed the high crystalline quality of these single crystals, illustrated by the diffuse map of the ($3\,K\,L$) reciprocal plane shown in Fig. 1(d), in which sharp Bragg reflections were observed in all three directions of the reciprocal space. The evolution of the lattice parameters as a function of Ca concentration as well as of a selection of internal structural degrees of freedom, especially the height of As, z_{As}, as the most relevant one, and the As-As distance along c, given by $(1 - 2 \times z_{As}) \times c$ are reported in Fig. 2. They show a relatively limited impact of Ca on the structure up to $x \sim 0.025$, where a slight increase of the a and c parameters can be seen. Above this concentration, a sizable contraction of these lattice parameters occurs. In parallel, we observe a continuous increase of z_{As} with the Ca concentration, alongside a trend toward a small decrease of the interlayer As-As distance. Consistent with our laboratory source data a similar decreasing trend in both a and c parameters with Ca content was observed when comparing the $x = 0.03$ and 0.08 samples studied with synchrotron radiation. The evaluation of other internal parameters, such as the Ni-As distance or the Ni-As-Ni bond angles, show very little dependence on Ca concentration, indicating little, if any, modification of the internal structure of the NiAs layers. Importantly, with increasing Ca concentration, the determination of the c-axis parameter becomes less reliable. Indeed, as illustrated in Fig. 3, where various diffuse scattering reciprocal space cuts for the $x = 0.03$ and 0.08 samples are shown, long streaks along the L direction appear in the out-of-plane reciprocal space cuts above $x > 0.04$. This indicates the presence of stacking faults in the structure for $x > 0.04$. These also produce potentially misleading finite intensities at forbidden Bragg reflections in cuts of reciprocal layers perpendicular to the streaks [e.g., some intensity is seen at the (1 1 1) position—marked by red arrows in Fig. 3(a)]. Overall, this results in a general degradation of the crystal periodic structure along the c axis, which limits the accuracy of the c lattice parameter estimate and of the internal structural parameters. It is in particular not possi-

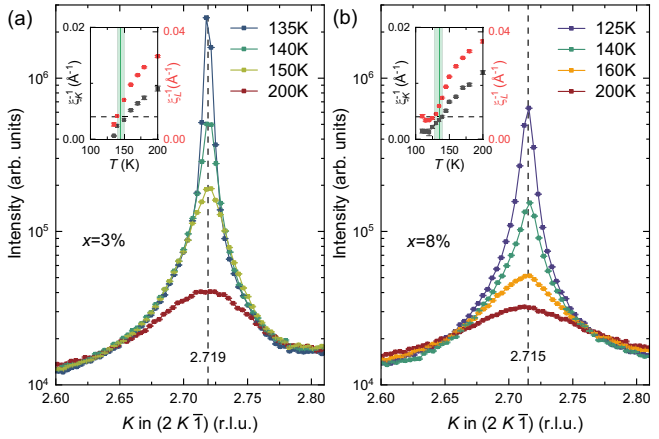

FIG. 4. Linecuts of the diffuse signal across $q_{\text{I-CDW}}$ along the $[0K0]$ direction at several temperatures. In (a) the I-CDW peak is shown at 200, 150, 140, and 135 K for an $x \sim 0.03$ sample. The vertical dashed line gives the K coordinate of the I-CDW peak center. The inset panel visualizes the inverse correlation length and the transition temperature T_{ICDW} in green, while the dashed line indicates the correlation length $\xi_{\text{K,L}} = 250, 120$ Å. In (b) the I-CDW peak of the $x \sim 0.08$ sample is presented in the same style.

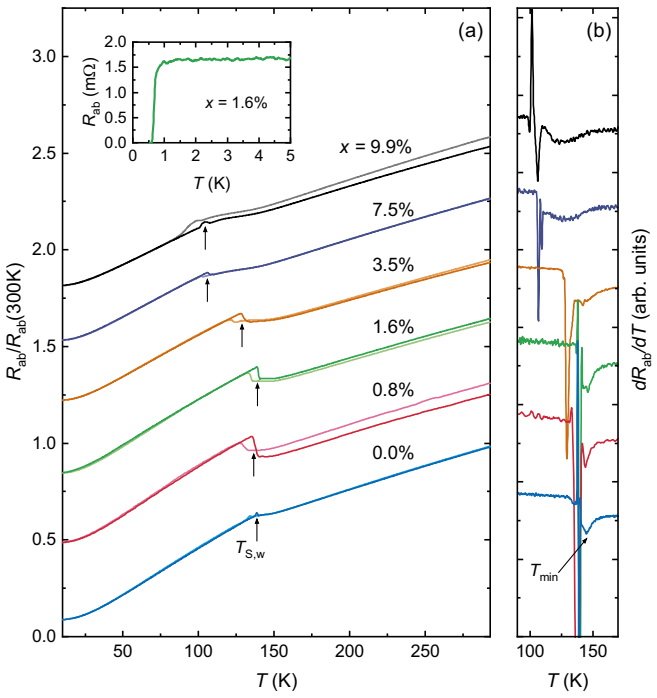

FIG. 5. (a) Temperature dependence of the in-plane electrical resistance of $Ba_{1-x}Ca_xNi_2As_2$, normalized by the room temperature value. The arrows indicate T_S on warming. The inset shows the resistance drop at the superconducting transition for $Ba_{1-x}Ca_xNi_2As_2$ with $x = 0.016$. (b) Temperature dependence of dR_{ab}/dT. The temperature of the local minimum T_{min} is indicated by an arrow for $BaNi_2As_2$. The curves are offset for clarity.

ble to discuss in detail the role of the c/a ratio, which has been reported in the $BaNi_2(As_{1-x}P_x)_2$ systems as an essential parameter controlling the electronic phase of this family of compounds [9]. Note that the reflections remain well defined in the H and K directions throughout the entire series. We have not detected signatures of parasitic phases or inclusions in the investigated samples, but we note that for those with higher x values, stronger variations of the Ca concentration from sample to sample within a given batch are reported with larger crystals pieces tending to be less homogeneous. EDX elemental maps on these samples did not show particular inhomogeneities in the Ca concentration over several tens of microns on a given terrace, but 0.01 to 0.02 variations of this concentration from one terrace to the next were routinely encountered [Fig. 1(c)]. The values given are best estimates from EDX and XRD.

B. Incommensurate and Commensurate CDWs

As previously reported for the parent compounds [12], a strong diffuse signal can already be seen at room temperature in the Ca-rich samples at reciprocal space wave vectors close to $q_{\text{I-CDW}} \sim (0.28\,0\,0)$, at which the I-CDW develops at lower temperatures. For all the investigated Ca concentrations, these develop into a long-range charge order, evidenced by the appearance of sharp Bragg-like reflections on top of the diffuse background upon cooling (Fig. 4). Using this criterion, we can estimate that the formation of the long-range I-CDW takes place at around 145 K for $x = 0.03$ and 135 K for $x = 0.08$. As shown in the insets of Fig. 4, in both compounds this occurs when the in-plane (resp. out-of-plane) correlation length reaches about $\xi_{\text{K}} \sim 250$ Å ($\xi_{\text{L}} \sim 120$ Å), comparable with a previous report on the parent compound [12]. We further note a small change in the incommensurability, where the ordering vector increases from $q = 0.281$ ($x = 0.03$) to $q = 0.285$ ($x = 0.08$). At the lowest temperature for which x-ray measurements were conducted (80 K), the I-CDW in all samples investigated in this study has evolved into a C-CDW with an ordering vector $q_{\text{C-CDW}} = (1/3\,0\,-1/3)$, which is—as for the undoped compound [8]—associated with the triclinic $P\bar{1}$ phase. No other superstructures were observed down to 80 K for ($x \leqslant 0.084$).

C. Phase transition temperatures

Next, we turn to electrical transport measurements, which are shown in Fig. 5(a). These reveal a metallic behavior at all Ca concentrations. For our pure $BaNi_2As_2$ single crystals, the residual resistance ratio RRR $= R_{ab}(300\,\text{K})/R_{ab}(T \to 0))$ is close to 12, indicating a high crystal quality in comparison to crystals previously grown by self-flux (RRR = 8 [16,35] and RRR = 5.5 [17]) or Pb-flux (RRR = 5 [5]). As the substitution level increases, RRR rapidly decreases to RRR = 6 at $x_{\text{Ca}} \sim 0.01$ (see Table II), before it stabilizes at about RRR = 4 up to the highest investigated concentrations. This is qualitatively in line with the comparably small in-plane disorder inferred from the x-ray measurements discussed above.

TABLE II. Residual resistance ratio RRR for several Ca substitutions x.

x(%)	0	0.8	1.3	1.6	3.5	7.5	9.4	9.9
RRR	11.8	5.9	5.2	4.9	3.8	4.0	4.4	4.4

Indeed, in all the investigated samples, a discontinuity in the resistance corresponding to the first-order transition to the triclinic phase (concomitant with the appearance of the C-CDW discussed above) can be seen at $T = T_S(x)$ [16,18]. This feature is highlighted even more upon evaluating the derivative of the resistivity dR/dT, see Fig. 5(b). At this transition, the lattice parameters change abruptly yielding the formation of cracks in the sample or at the electrical contacts, which may offset the resistance [see the discrepancy between the cooling and warming curves in Fig. 5(a)]. More interesting is the Ca concentration dependence of the transition temperature $T_S(x)$. Following the trend observed in the lattice parameters, T_S displays only small changes up to $x \sim 0.02$, before starting to rapidly decrease. As previously noted [10] a local minimum in dR_{ab}/dT is seen at $T_{\min}$, a few K above T_S at a temperature comparable to that, at which the long-range I-CDW forms. Our experimental setup for electrical transport did not allow us to explore the superconducting transition systematically, but we could detect it in a $x = 0.016$ crystal at $T_c \sim 0.7$ K, a temperature slightly above that of the pristine material.

To gain additional insights on the Ca concentration dependence of T_c and of the structural phase transitions in $Ba_{1-x}Ca_xNi_2As_2$, we have looked for their thermodynamic signatures by performing specific heat measurements in the temperature range from 300 K to 0.4 K. Figure 6(a) shows the specific heat C_p for a $Ba_{1-x}Ca_xNi_2As_2$ sample with $x = 0.034$ from room temperature down to 2 K. At a high temperature, the C_p saturates at the Dulong-Petit limit (see green dashed line) [36]. The first-order triclinic transition manifests as a pronounced peak [9,10,16], showing a hysteretic behavior at temperatures that are in excellent agreement with T_S inferred from transport and x-ray measurements discussed in the previous sections. Note that the limited size of the crystals available did not allow us to resolve the specific heat jump associated with the second-order transition of the tetragonal to the (minute) orthorhombic distortion evidenced in P-substituted compounds [9] as the long-range I-CDW forms [12].

Additionally, we have extracted the Sommerfeld coefficient γ and the Debye temperature Θ_D by fitting the low-temperature range from 2 K to 8 K to a second-order polynomial $C_p(T)/T = \gamma + \beta T^2 + \alpha T^4$.

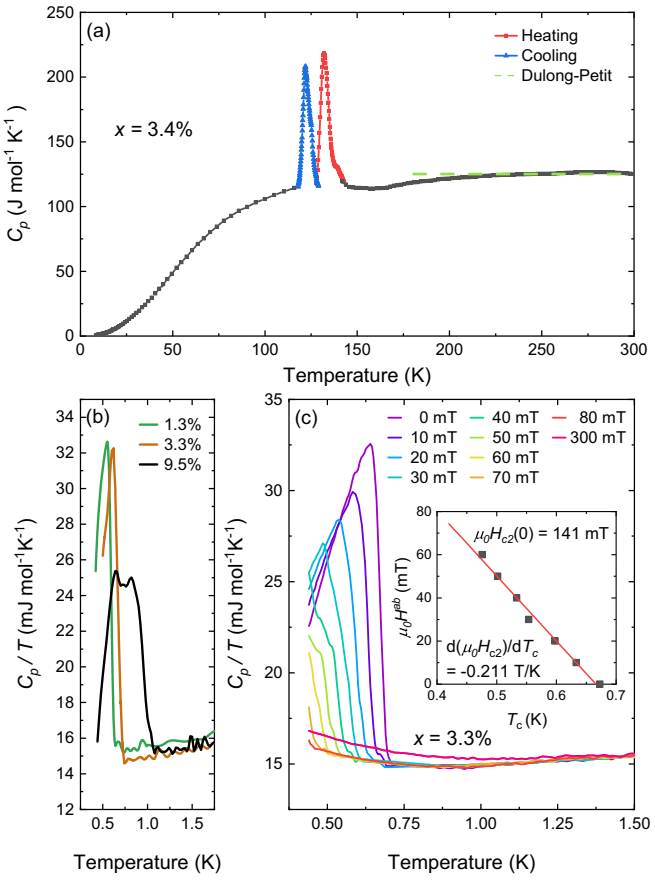

FIG. 6. (a) Temperature dependence of the specific heat of $Ba_{1-x}Ca_xNi_2As_2$ for a sample with $x = 0.034$. The blue line indicates the first-order transition peak at $T_{S,c} \sim 124$ K on cooling, the red one at $T_{S,w} \sim 135$ K on warming. At a high temperature, C_p reaches the Dulong-Petit limit $\sim 3 p_{uc} k_B$ (with k_B being the Boltzmann constant and p_{uc} the number of atoms per unit cell), that is depicted by the green dashed line. (b) C_p/T at low temperature. The discontinuity indicates bulk superconductivity below 0.6 K, 0.7 K, and 1 K for $x = 0.013$, 0.033, and 0.095, respectively. (c) C_p/T vs T with varying in-plane magnetic field for a $Ba_{1-x}Ca_xNi_2As_2$ sample with $x = 0.033$. The inset shows the extracted T_c as a function of the applied magnetic field, fitted linearly by the red line.

D. Superconducting properties

At low temperatures, a second-order phase transition marks the onset of superconductivity. The superconducting transition temperature T_c is determined by applying the entropy-conserving construction [37]. In Fig. 6(b), $C_p(T)/T$ is shown below 1.75 K for three $Ba_{1-x}Ca_xNi_2As_2$ samples with different Ca content. The specific heat jump of Ca substituted samples occurs at a slightly higher temperature than in the parent compound, confirming T_c obtained from the low-temperature resistivity [see inset Fig. 5(a)]. While the increase of T_c with x is weak but systematic, $\Delta C/(\gamma T_c) \sim 1.4$ remains essentially constant in the substitution range $x \leqslant 0.033$. This is in good agreement with the undoped compound as well as with standard weak-coupling BCS theory [38]. For high substitution levels, we observe that the onset of the superconducting transition temperature is significantly increased, while the transition broadens substantially compared to lower substitution levels. It could in fact be interpreted as two sharp superconducting transitions with respective T_c of about 0.7 K and 1.0 K (considering only the later onset naturally yields a decrease of the $\Delta C/(\gamma T_c)$ ratio). This is again consistent with inhomogeneous Ca distribution for $x > 0.04$ samples.

The T_c, γ, Θ_D and $\Delta C/(\gamma T_c)$ extracted from our analysis are summarized together with the samples' respective Ca content and mass in Table III. The Debye temperature increases slowly with Ca concentration, in contrast with the observations reported in the cases of Sr [17], Cu [39], and P [16] substitutions, where the Θ_D remains essentially constant before reducing notably following the suppression of the triclinic phase. Conversely, in the case of Co [40] substitutions, Θ_D exhibits minimal change across the entire doping series. The Sommerfeld coefficient γ on the other hand appears essentially independent of the Ca concentration, akin to observation made in the cases of Cu and P substitutions, but

TABLE III. Superconducting transition temperature T_c, Sommerfeld coefficient γ, Debye temperature Θ_D, and the ratio $\Delta C/(\gamma T_c)$ of several $Ba_{1-x}Ca_xNi_2As_2$ samples with mass m. The first row shows results from [35], the second from [16].

x	m (mg)	T_c (K)	γ (mJ/mol K^2)	Θ_D (K)	$\Delta C/\gamma\, T_c$
0.0		0.7	13.2	250	1.38
0.0		0.6	14.0	250	1.30
0.013	3.45	0.6	14.8	275	1.36
0.033	2.77	0.7	14.4	280	1.40
0.095	1.07	1.0	14.3	260	0.78

in contrast with Co and Sr substitutions, which respectively slightly increase and decrease γ.

Finally, we discuss the field dependence of the superconducting transition temperature by looking at the low-temperature specific heat of a $x = 0.033$ sample with an in-plane applied magnetic field [see Fig. 6(c)]. The resulting $T_c(\mu_0 H)$ is plotted in the inset. From a linear fit we obtain an upper critical field slope of $d(\mu_0 H_{c2})/dT_c = -0.211\,\mathrm{T/K}$, which is similar to that of the pristine $BaNi_2As_2$ ($-0.396\,\mathrm{T/K}$ [5], $-0.226\,\mathrm{T/K}$ [14]), but much smaller than what is observed in iron-based superconductors, where $d(\mu_0 H_{c2})/dT_c \sim -5\,\mathrm{T/K}$ [41–43]. We can then estimate $H_{c2}(0)$ with $H(T_c) = 0.7 \cdot (H_{c2}(0) - dH_{c2}/dT_c \cdot T_c)$ [44], which results in an upper critical field of $\mu_0 H_{c2}(0) = 141\,\mathrm{mT}$ again similar to $BaNi_2As_2$ [5].

V. DISCUSSION

We start our discussion by summarizing our experimental results in the phase diagram shown in Fig. 7. After a small initial increase, $T_{S,c}$ (measured on cooling, hereafter referred to as T_S) decreases continuously from about 137 K to below 100 K. In the entire substitution range investigated in this work, the phase transition into the triclinic phase remains hysteretic and first order. Above it, we detect an I-CDW phase similar to that of the parent compound, with a small increase in the incommensurate ordering vector $q_{\text{I-CDW}}$ with x.At low temperatures, our thermodynamic and transport measurements detect a superconducting transition at a temperature that increases with Ca content from 0.6 K to 1 K. No additional structural or electronic phases were detected in the investigated substitution range. The decrease of T_S with increasing Ca concentration we report is qualitatively similar to the effects observed upon P substitution on the As site, or Sr substitution on the Ba site [9,16,17]. Focusing on the Ba-site substitutions, we note that quantitatively Ca substitutions are significantly more effective in suppressing T_S than Sr. Indeed, $T_S = 120\,\mathrm{K}$ is reached with only $x_{Ca} \sim 0.035$, while Sr concentration of $x_{Sr} \sim 0.3$ are needed. Similarly, we reached $T_S = 100\,\mathrm{K}$ with $x_{Ca} \sim 0.09$, which would take $x_{Sr} \sim 0.5$ [17]. A simple extrapolation, shown in Fig. 7, suggests that a concentration between 0.15 and 0.2 of Ca would be sufficient to suppress completely the triclinic/C-CDW phase. Given that these substitutions are isovalent, this difference cannot be attributed to charge-doping effects. Furthermore, since the most efficient suppression is achieved in the system requiring the least amount of substitution, we can

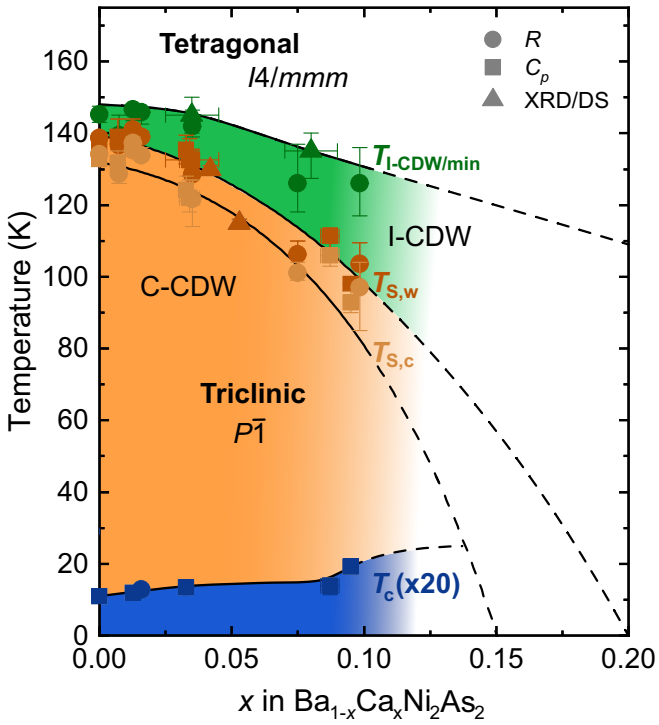

FIG. 7. Phase diagram of $Ba_{1-x}Ca_xNi_2As_2$ up to a substitution level of about $x = 0.1$. Circles represent results from electrical transport, squares from specific heat, and triangles from XRD and DS measurements. The dashed line shows a simple extrapolation of the transition temperature dependence on Ca content indicating that complete suppression of the C-CDW should occur between 0.15 and 0.2.

conclude that the rate of T_S decrease is not controlled by the associated cationic disorder. In comparison to the Sr case, which mostly impacts the c axis, while leaving a barely affected up to $x_{Sr} \sim 0.7$ [17], a contraction of both a- and c-axis lattice parameters can be seen already from $x_{Ca} \sim 0.03$. This suggests that the modifications induced by Ca substitutions in $BaNi_2As_2$ are most likely rooted in chemical pressure effects. Along this line, we note that Ca-doping of the Ba site appears unique since it preserves the NiAs layers, and both, c and a, (globally) decrease, mimicking the effect of hydrostatic pressure. A direct comparison of the relative lattice parameters' changes induced by pressure [11] indicates that 0.03 of Ca have the same effect on the sample unit cell as ∼0.5 GPa of hydrostatic pressure. The rather weak dependence of the onset temperature of the I-CDW transition and the increase of the ordering vector $q_{\text{I-CDW}}$ from 0.28 to 0.285 at $x = 0.08$ are indeed comparable to the effect of a hydrostatic compression of ∼1.5 GPa [11].

This analogy between the effects of pressure and Ca substitution warrants further investigation, particularly concerning their respective influence on the electronic structure. In Fig. 8, we compare the calculated band structure of $BaNi_2As_2$—which shows excellent agreement with previous reports [24]—to that under 10 GPa of hydrostatic pressure and that of $CaNi_2As_2$. Among the numerous modifications, we note a pronounced upward shift of the innermost electron pockets at the X and P points of the first Brillouin zone, as

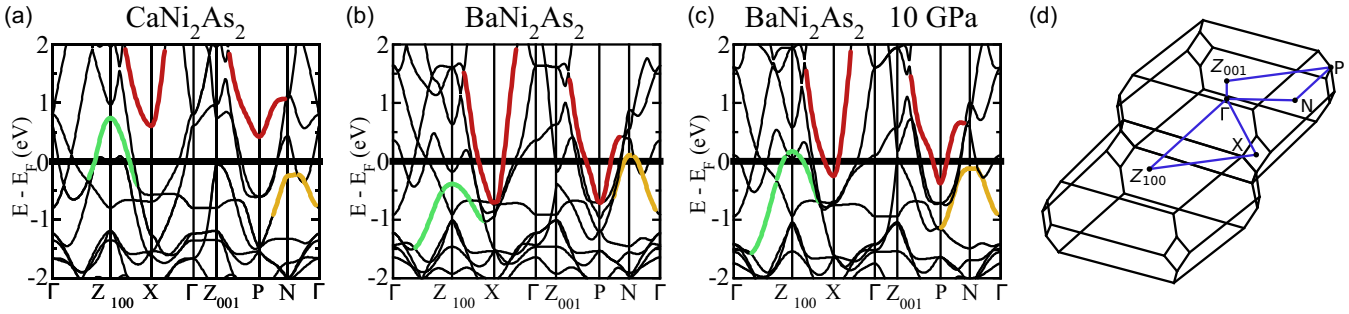

FIG. 8. (a) Calculated band structure $CaNi_2As_2$, (b) $BaNi_2As_2$, and (c) $BaNi_2As_2$ under 10 GPa of hydrostatic pressure with the most important differences highlighted. The innermost electron pockets at the X and P points of the first Brillouin zone (red) and the hole pocket around the Z_{100} (green) involve strongly hybridized As p_z and Ni d_{z^2} states. The hole pocket at the N-point (yellow) originates from the Ni-d_{xy} orbitals, with d_{xz}/d_{yz} character near the band top. (d) The $BaNi_2As_2$ Brillouin zone with high symmetry points marked, generated with a tool based on [45] and [46].

well as a similar shift in a hole pocket around the Z_{100}, both induced by pressure and Ca substitution. These changes in the Fermi surface topology predominantly involve strongly hybridized As p_z and Ni d_{z^2} states and are likely linked to the intricate pressure-temperature phase diagrams of these materials [11] which host multiple competing instabilities. Notably, we also observe the suppression of a hole pocket at the N point of the reciprocal space, which originates from the Ni-d_{xy} orbitals, with d_{xz}/d_{yz} character near the band top. This feature leaves the Fermi level under both Ca substitution and pressure, reinforcing recent discussions on the role of fluctuations in the occupation of the d_{xz} and d_{yz} orbitals in CDW formation [8] and the emergence of a nematic liquid state [10]. Furthermore, similar behavior has been reported in $Ba_{1-x}Sr_xNi_2As_2$, where the Lifshitz transition associated with the disappearance of these states from the Fermi level coincides with a marked enhancement of nematic fluctuations and the maximum superconducting T_c [24]. Experimentally, however, our specific heat results [Fig. 6(c)] indicate that within this doping range superconductivity remains in the weak-coupling BCS limit. Nonetheless, the suppression of T_S and the small increase of the superconducting T_c upon Ca substitution are stronger than the reported effects of pressure [47] and reminiscent of the Sr- and P-substituted cases. Importantly, given the large B_{1g} elastoresistance signal, whose possible electronic nematic origin is debated [9,17,18] in Sr- and P-substituted systems, similar investigations also call for Ca-substituted systems. Although no such experiments have been performed yet, the strong similarity of freestanding electrical resistance of Ca- and P-substituted samples strongly suggests a similar behavior. Finally, the limited doping range investigated did not allow us to fully suppress the coincident C-CDW and triclinic phase transition, where T_c has been reported to sharply increase to ∼3K in P- [9,16] or Sr- [17] substituted samples. An optimization of the growth conditions appears needed to reach these optimal conditions for superconductivity while avoiding stacking faults. This might be improved by increasing the growth temperature above 1250 °C, calling for the use of alternative growth conditions (crucible material, gas pressure, etc.). Furthermore, the increased vapor pressure of binary arsenides, CaAs, and NiAs used in the growth at these elevated temperatures probably require high-pressure synthesis similar to that used for $BaNi_2P_2$ [48,49].

VI. SUMMARY

In conclusion, we report the growth and a detailed investigation of $Ba_{1-x}Ca_xNi_2As_2$ single crystals, up to $x \sim 0.1$. Upon Ca substitution, akin to earlier studies on Sr- and P-substituted samples, the triclinic and associated C-CDW transition are suppressed while the superconducting one is enhanced. In contrast, and especially compared to the effect of Sr substitution, which also occurs on the Ba site, the effect of Ca on the crystal structure appears to be much closer to that of hydrostatic pressure [11]. As a consequence, the amount of Ca required to suppress the triclinic transition temperature is significantly lower than that of Sr, opening a promising avenue to study the possible nematicity of the compound at a lower disorder level. Our thermodynamic measurements strongly suggest that, within the entire range investigated, superconductivity remains of weak-coupling BCS type. However, for $x_{Ca} \geqslant 0.04$ we observe evidence of significant stacking fault formation, which limits the range of our investigations and in particular the relevance of the c/a ratio in phase tuning. While this observation calls for the optimization of the growth conditions, we stress that this should not preclude investigating the possible electronic nematicity of $Ba_{1-x}Ca_xNi_2As_2$.

ACKNOWLEDGMENTS

Fruitful discussions with F. Hardy, C. Meingast, and S.-M. Souliou are gratefully acknowledged. We acknowledge support of the Deutsche Forschungsgemeinschaft (DFG; German Research Foundation) under CRC/TRR 288 (Project No. B03). We acknowledge the European Synchrotron Radiation Facility (ESRF) for the provision of synchrotron radiation facilities under Proposal No. HC-4946. K.W. acknowledges support from the Swiss National Science Foundation through the Postdoc. Mobility program. M.F. acknowledges funding from the Alexander von Humboldt Foundation and the Young Investigator Group preparatory program of the Karlsruhe Institute of Technology. R.H. acknowledges support of the state of Baden-Württemberg through bwHPC.

DATA AVAILABILITY

The data that support the findings of this article are openly available [50].

[1] R. M. Fernandes, P. P. Orth, and J. Schmalian, Intertwined vestigial order in quantum materials: Nematicity and beyond, Annu. Rev. Condens. Matter Phys. **10**, 133 (2019).

[2] D. N. Basov, R. D. Averitt, and D. Hsieh, Towards properties on demand in quantum materials, Nat. Mater. **16**, 1077 (2017).

[3] B. Keimer, S. A. Kivelson, M. R. Norman, S. Uchida, and J. Zaanen, From quantum matter to high-temperature superconductivity in copper oxides, Nature (London) **518**, 179 (2015).

[4] G. R. Stewart, Superconductivity in iron compounds, Rev. Mod. Phys. **83**, 1589 (2011).

[5] F. Ronning, N. Kurita, E. D. Bauer, B. L. Scott, T. Park, T. Klimczuk, R. Movshovich, and J. D. Thompson, The first order phase transition and superconductivity in $BaNi_2As_2$ single crystals, J. Phys.: Condens. Matter **20**, 342203 (2008).

[6] S. Lee, G. de la Peña, S. X. L. Sun, M. Mitrano, Y. Fang, H. Jang, J.-S. Lee, C. Eckberg, D. Campbell, J. Collini, J. Paglione, F. M. F. de Groot, and P. Abbamonte, Unconventional charge density wave order in the pnictide superconductor $Ba(Ni_{1-x}Co_x)_2As_2$, Phys. Rev. Lett. **122**, 147601 (2019).

[7] S. Lee, J. Collini, S. X. L. Sun, M. Mitrano, X. Guo, C. Eckberg, J. Paglione, E. Fradkin, and P. Abbamonte, Multiple charge density waves and superconductivity nucleation at antiphase domain walls in the nematic pnictide $Ba_{1-x}Sr_xNi_2As_2$, Phys. Rev. Lett. **127**, 027602 (2021).

[8] M. Merz, L. Wang, T. Wolf, P. Nagel, C. Meingast, and S. Schuppler, Rotational symmetry breaking at the incommensurate charge-density-wave transition in $Ba(Ni, Co)_2(As, P)_2$: Possible nematic phase induced by charge/orbital fluctuations, Phys. Rev. B **104**, 184509 (2021).

[9] C. Meingast, A. Shukla, L. Wang, R. Heid, F. Hardy, M. Frachet, K. Willa, T. Lacmann, M. Le Tacon, M. Merz, A.-A. Haghighirad, and T. Wolf, Charge density wave transitions, soft phonon, and possible electronic nematicity in $BaNi_2(As_{1-x}P_x)_2$, Phys. Rev. B **106**, 144507 (2022).

[10] Y. Yao, R. Willa, T. Lacmann, S.-M. Souliou, M. Frachet, K. Willa, M. Merz, F. Weber, C. Meingast, R. Heid, A.-A. Haghighirad, J. Schmalian, and M. Le Tacon, An electronic nematic liquid in $BaNi_2As_2$, Nat. Commun. **13**, 4535 (2022).

[11] T. Lacmann, A.-A. Haghighirad, S.-M. Souliou, M. Merz, G. Garbarino, K. Glazyrin, R. Heid, and M. Le Tacon, High-pressure phase diagram of $BaNi_2As_2$: Unconventional charge density waves and structural phase transitions, Phys. Rev. B **108**, 224115 (2023).

[12] S. M. Souliou, T. Lacmann, R. Heid, C. Meingast, M. Frachet, L. Paolasini, A. A. Haghighirad, M. Merz, A. Bosak, and M. Le Tacon, Soft-phonon and charge-density-wave formation in nematic $BaNi_2As_2$, Phys. Rev. Lett. **129**, 247602 (2022).

[13] Y. Song, S. Wu, X. Chen, Y. He, H. Uchiyama, B. Li, S. Cao, J. Guo, G. Cao, and R. Birgeneau, Phonon softening and slowing-down of charge density wave fluctuations in $BaNi_2As_2$, Phys. Rev. B **107**, L041113 (2023).

[14] N. Kurita, F. Ronning, Y. Tokiwa, E. D. Bauer, A. Subedi, D. J. Singh, J. D. Thompson, and R. Movshovich, Low-temperature magnetothermal transport investigation of a Ni-based superconductor $BaNi_2As_2$: Evidence for fully gapped superconductivity, Phys. Rev. Lett. **102**, 147004 (2009).

[15] J. Collini, D. J. Campbell, D. Sneed, P. Saraf, C. Eckberg, J. Jeffries, N. Butch, and J. Paglione, Charge order evolution of superconducting $BaNi_2As_2$ under high pressure, Phys. Rev. B **108**, 205103 (2023).

[16] K. Kudo, M. Takasuga, Y. Okamoto, Z. Hiroi, and M. Nohara, Giant phonon softening and enhancement of superconductivity by phosphorus doping of $BaNi_2As_2$, Phys. Rev. Lett. **109**, 097002 (2012).

[17] C. Eckberg, D. J. Campbell, T. Metz, J. Collini, H. Hodovanets, T. Drye, P. Zavalij, M. H. Christensen, R. M. Fernandes, S. Lee, P. Abbamonte, J. W. Lynn, and J. Paglione, Sixfold enhancement of superconductivity in a tunable electronic nematic system, Nat. Phys. **16**, 346 (2020).

[18] M. Frachet, P. Wiecki, T. Lacmann, S. M. Souliou, K. Willa, C. Meingast, M. Merz, A. A. Haghighirad, M. Le Tacon, and A. E. Böhmer, Elastoresistivity in the incommensurate charge density wave phase of $BaNi_2(As_{1-x}P_x)_2$, npj Quantum Mater. **7**, 115 (2022).

[19] A. Subedi and D. J. Singh, Density functional study of $BaNi_2As_2$: Electronic structure, phonons, and electron-phonon superconductivity, Phys. Rev. B **78**, 132511 (2008).

[20] L. Song, J. Si, T. Fennell, U. Stuhr, G. Deng, J. Wang, J. Liu, L. Hao, H. Luo, M. Liu, S. Meng, and S. Li, Strong electron-phonon coupling in $Ba_{1-x}Sr_xNi_2As_2$, Phys. Rev. B **109**, 104518 (2024).

[21] T. Noda, K. Kudo, M. Takasuga, M. Nohara, T. Sugimoto, D. Ootsuki, M. Kobayashi, K. Horiba, K. Ono, H. Kumigashira, A. Fujimori, N. L. Saini, and T. Mizokawa, Orbital-dependent band renormalization in $BaNi_2(As_{1-x}P_x)_2$ ($x = 0.00$ and 0.092), J. Phys. Soc. Jpn. **86**, 064708 (2017).

[22] A. Kreyssig, M. A. Green, Y. Lee, G. D. Samolyuk, P. Zajdel, J. W. Lynn, S. L. Bud'ko, M. S. Torikachvili, N. Ni, S. Nandi, J. B. Leão, S. J. Poulton, D. N. Argyriou, B. N. Harmon, R. J. McQueeney, P. C. Canfield, and A. I. Goldman, Pressure-induced volume-collapsed tetragonal phase of $CaFe_2As_2$ as seen via neutron scattering, Phys. Rev. B **78**, 184517 (2008).

[23] A. Mewis and A. Distler, Zur Kenntnis der Verbindungen $CaNi_2As_2$, $SrNi_2As_2$ und $Ca_{2,3}Ni_{11,7}As_7$ / on the compounds $CaNi_2As_2$, $SrNi_2As_2$, and $Ca_{2,3}Ni_{11,7}As_7$, Zeitschrift für Naturforschung B **35**, 391 (1980).

[24] D. M. Narayan, P. Hao, R. Kurleto, B. S. Berggren, A. G. Linn, C. Eckberg, P. Saraf, J. Collini, P. Zavalij, M. Hashimoto, D. Lu, R. M. Fernandes, J. Paglione, and D. S. Dessau, Potential lifshitz transition at optimal substitution in nematic pnictide $Ba_{1-x}Sr_xNi_2As_2$, Sci. Adv. **9**, eadi4966 (2023).

[25] Rigaku Oxford Diffraction Ltd, Yarnton, Oxfordshire, E 2015 CrysAlis PRO (2015).

[26] G. M. Sheldrick, A short history of *SHELX*, Acta Crystallogr. A: Found Crystallogr. **64**, 112 (2008).

[27] V. Petříček, M. Dušek, and L. Palatinus, Crystallographic computing system JANA2006: General features, Z. Kristallogr. Cryst. Mater. **229**, 345 (2014).

[28] A. Girard, T. Nguyen-Thanh, S. Souliou, M. Stekiel, W. Morgenroth, L. Paolasini, A. Minelli, D. Gambetti, B. Winkler, and A. Bosak, A new diffractometer for diffuse scattering studies on the ID28 beamline at the esrf, J. Synchrotron Radiat. **26**, 272 (2019).

[29] S. G. Louie, K.-M. Ho, and M. L. Cohen, Self-consistent mixed-basis approach to the electronic structure of solids, Phys. Rev. B **19**, 1774 (1979).

[30] B. Meyer, C. Elsässer, and M. Fähnle, Fortran90 program for mixed-basis pseudopotential calculations for crystals

(1997), Max-Planck-Institut für Metallforschung, Stuttgart (unpublished).

[31] D. R. Hamann, M. Schlüter, and C. Chiang, Norm-conserving pseudopotentials, Phys. Rev. Lett. **43**, 1494 (1979).

[32] G. B. Bachelet, D. R. Hamann, and M. Schlüter, Pseudopotentials that work: From H to Pu, Phys. Rev. B **26**, 4199 (1982).

[33] D. Vanderbilt, Optimally smooth norm-conserving pseudopotentials, Phys. Rev. B **32**, 8412 (1985).

[34] J. P. Perdew, K. Burke, and M. Ernzerhof, Generalized gradient approximation made simple, Phys. Rev. Lett. **77**, 3865 (1996).

[35] A. S. Sefat, M. A. McGuire, R. Jin, B. C. Sales, D. Mandrus, F. Ronning, E. D. Bauer, and Y. Mozharivskyj, Structure and anisotropic properties of $BaFe_{2-x}Ni_xAs_2$ ($x = 0$, 1, and 2) single crystals, Phys. Rev. B **79**, 094508 (2009).

[36] P. L. Dulong and A.-T. Petit, Recherches sur quelques points importants de la Théorie de la Chaleur, Annales de Chimie et de Physique **10**, 395 (1819).

[37] K. Willa, R. Willa, K. W. Song, G. D. Gu, J. A. Schneeloch, R. Zhong, A. E. Koshelev, W.-K. Kwok, and U. Welp, Nanocalorimetric evidence for nematic superconductivity in the doped topological insulator $Sr_{0.1}Bi_2Se_3$, Phys. Rev. B **98**, 184509 (2018).

[38] J. Bardeen, L. N. Cooper, and J. R. Schrieffer, Theory of superconductivity, Phys. Rev. **108**, 1175 (1957).

[39] K. Kudo, M. Takasuga, and M. Nohara, Copper doping of $BaNi_2As_2$: Giant phonon softening and superconductivity enhancement, arXiv:1704.04854.

[40] C. Eckberg, L. Wang, H. Hodovanets, H. Kim, D. J. Campbell, P. Zavalij, P. Piccoli, and J. Paglione, Evolution of structure and superconductivity in $Ba(Ni_{1-x}Co_x)_2As_2$, Phys. Rev. B **97**, 224505 (2018).

[41] F. Hardy, L. Doussoulin, T. Klein, M. He, A. Demuer, R. Willa, K. Willa, A. A. Haghighirad, T. Wolf, M. Merz, C. Meingast, and C. Marcenat, Vortex-lattice melting and paramagnetic depairing in the nematic superconductor FeSe, Phys. Rev. Res. **2**, 033319 (2020).

[42] K. Willa, R. Willa, J. K. Bao, A. E. Koshelev, D. Y. Chung, M. G. Kanatzidis, W. K. Kwok, and U. Welp, Strongly fluctuating moments in the high-temperature magnetic superconductor $RbEuFe_4As_4$, Phys. Rev. B **99**, 180502 (2019).

[43] R. Prozorov, V. G. Kogan, M. Kończykowski, and M. A. Tanatar, Slope of the upper critical field at T_c in two-band superconductors with nonmagnetic disorder: s_{++} superconductivity in $Ba_{1-x}K_xFe_2As_2$, Phys. Rev. B **109**, 024506 (2024).

[44] N. R. Werthamer, E. Helfand, and P. C. Hohenberg, Temperature and purity dependence of the superconducting critical field, H_{c2}. III. Electron spin and spin-orbit effects, Phys. Rev. **147**, 295 (1966).

[45] Y. Hinuma, G. Pizzi, Y. Kumagai, F. Oba, and I. Tanaka, Band structure diagram paths based on crystallography, Comput. Mater. Sci. **128**, 140 (2017).

[46] A. Togo, K. Shinohara, and I. Tanaka, Spglib: A software library for crystal symmetry search, Sci. Technol. Adv. Mate. **4**, 2384822 (2024).

[47] T. Park, H. Lee, E. D. Bauer, J. D. Thompson, and F. Ronning, Pressure dependence of $BaNi_2As_2$, J. Phys.: Conf. Ser. **200**, 012155 (2010).

[48] H. Kito, H. Eisaki, and A. Iyo, Superconductivity at 54 k in f-free $NdFeAsO_{1-y}$, J. Phys. Soc. Jpn. **77**, 063707 (2008).

[49] Y. Tomioka, T. Ito, H. Kito, A. Iyo, H. Eisaki, S. Ishida, M. Nakajima, and S.-i. Uchida, A resistive transition between the normal and superconducting state of $BaNi_2P_2$ single crystals, J. Phys. Soc. Jpn. **77**, 136 (2008).

[50] F. Henssler, K. Willa, M. Frachet, T. Lacmann, D. A. Chaney, R. Heid, M. Merz, A.-A. Haghighirad, and M. Le Tacon, Impact of Ca Substitution on Competing Orders in Superconducting $BaNi_2As_2$, Karlsruhe Institute of Technology (2025), https://radar.kit.edu/radar/en/dataset/psd333qp4z5yjpdj.